Orientation Analysis of Simulated Tornadic Debris

ARTURO UMEYAMA AND BOON LENG CHEONG

Advanced Radar Research Center, University of Oklahoma, Norman, Oklahoma

SEBASTIÁN TORRES

Cooperative Institute for Mesoscale Meteorological Studies, University of Oklahoma, and NOAA/OAR/National Severe Storms Laboratory, Norman, Oklahoma

DAVID BODINE

Advanced Radar Research Center, University of Oklahoma, Norman, Oklahoma

(Manuscript received 22 August 2017, in final form 11 February 2018)

ABSTRACT

Polarimetric weather radars are capable of detecting tornadic debris signatures (TDSs), which result from debris being lofted to the level of the radar beam and can be modulated by centrifuging and debris fallout. TDSs have been used in promising applications, such as enhanced tornado detection, improved warning and assessment of a potential tornado threat, and estimating tornado damage potential and intensity. Regions with negative differential reflectivity Z_{DR} have been found in TDS observations but a physical explanation is yet to be determined. Some hypotheses suggest a common alignment of debris or non-Rayleigh scattering to be the cause. However, because it is inherently difficult and extremely dangerous to verify this, a simulated environment can aid in this context to reveal information that would otherwise be impossible to retrieve in practice. Under the simulation environment, the true construct of the debris is known, wherefrom the bulk distributions of position and orientation data can be extracted for statistical analysis. The primary focus of this work is to investigate the cause of nonzero mean values of Z_{DR} in TDSs with simulated data from SimRadar, which is a polarimetric radar time series simulator developed for tornadic debris studies. The 6-degrees-of-freedom (DOF) model shows that for both small and large platelike debris, the debris face tends to have some common degree of alignment normal to the wind direction, which may be a plausible cause for the occurrence of negative Z_{DR} in real polarimetric radar observations. Potential explanations for other hypotheses regarding tornado and debris dynamics are also briefly discussed.

1. Introduction

Polarimetric radars are useful for the remote sensing of the atmosphere, particularly in situations where it would be extremely dangerous or impossible to perform in situ measurements (Snyder and Bluestein 2014), and are an efficient tool for classifying and discriminating between different meteorological and nonmeteorological scatterers (e.g., Zrnić and Ryzhkov 1999; Vivekanandan et al. 1999). Polarimetric observations have shown evidence of tornadic debris signatures (TDSs), which may effectively complement Doppler data (Ryzhkov et al. 2005) to aid in tornado-related applications by observing changes in the tornadic debris field (Bodine et al. 2011). This is particularly useful for cases in which traditional tornado-warning criteria are absent or overlooked (when ground observations are not possible, e.g., tornadoes in heavy rain or at night; or, when low-level velocity data are unavailable, e.g., at long ranges), and could allow the issuance of more specific statements or tornado emergencies (Ryzhkov et al. 2005; Bodine et al. 2013).

TDSs (Fig. 1) are tornado-scale polarimetric signatures collocated with a tornado that is lofting debris particles to the level of the radar beam (Ryzhkov et al. 2005). Since debris particles may have random orientations, irregular shapes, and a wide range of sizes and

Supplemental information related to this paper is available at the Journals Online website: https://doi.org/10.1175/JTECH-D-17-0140.s1.

Corresponding author: Arturo Umeyama, aumeyama@ou.edu

DOI: 10.1175/JTECH-D-17-0140.1

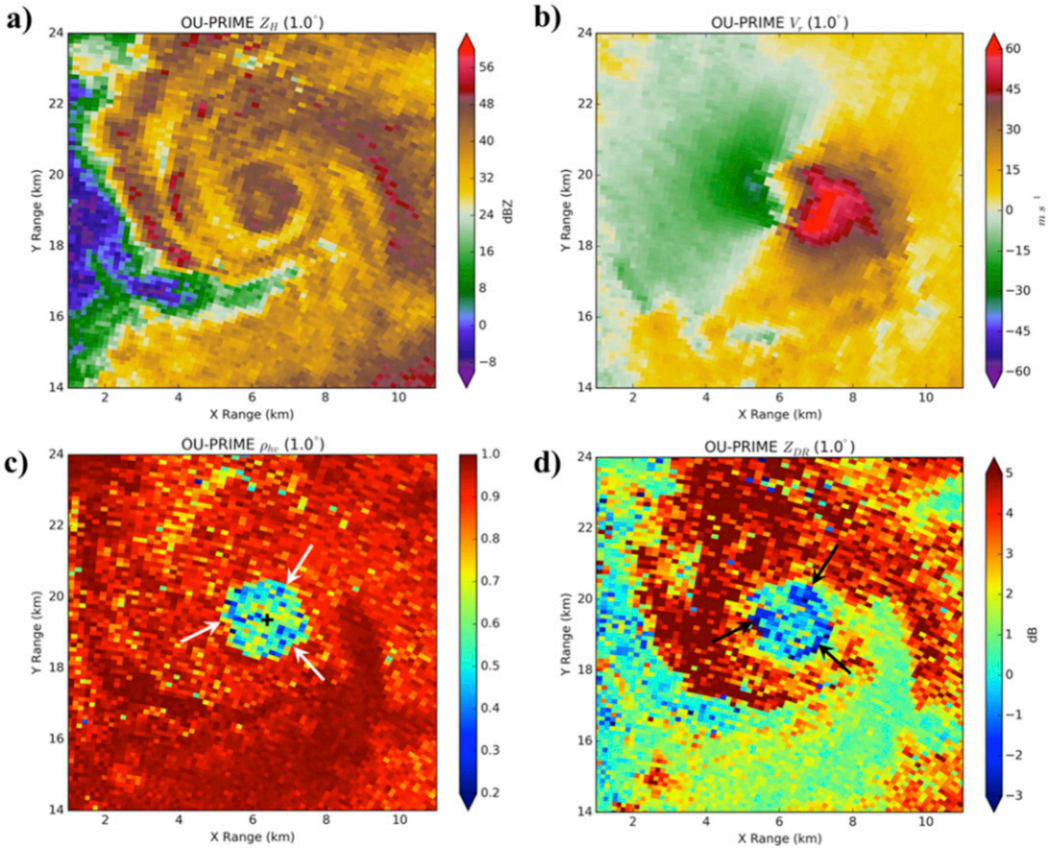

FIG. 1. An example of a TDS seen in the 10 May 2010 Moore–Choctaw, OK, tornado, data from the University of Oklahoma's (OU) Polarimetric Radar for Innovations in Meteorology and Engineering (PRIME) radar at 2231 UTC and $\phi = 1.0°$, at approximately 400 m above radar level. (a) Z_H, (b) $\overline{v}_r$, (c) ρ_{HV}, and (d) Z_{DR}. The arrows in (c) and (d) indicate the pockets of low ρ_{HV} and Z_{DR}, and the cross in (c) indicates the subjectively determined TDS center. Extracted from Griffin et al. (2017) with permission.

dielectric constants, they produce distinctive polarimetric characteristics in radar observations (e.g., Ryzhkov et al. 2005; Bluestein et al. 2007; Kumjian and Ryzhkov 2008; Snyder et al. 2010; Palmer et al. 2011; Bodine et al. 2011; Bunkers and Baxter 2011). Different criteria have been established to determine the likelihood of a radar resolution volume containing debris. A typical TDS, at typical weather radar frequencies, is associated with low-to-high reflectivity factor Z_H, low differential reflectivity Z_{DR}, and low copolar correlation coefficient ρ_{HV} (Ryzhkov et al. 2005; Schultz et al. 2012a,b; Bodine et al. 2013).

Because TDSs are repeatable features in tornadoes that are lofting sufficient debris (Kumjian and Ryzhkov 2008; Bodine et al. 2011, 2013), they provide promising application in tornado detection (Ryzhkov et al. 2005; Scharfenberg et al. 2005), confirmation of tornado warnings (Schultz et al. 2012a,b), and near-real-time estimation of tornado intensity and damage potential (Bodine et al. 2013; Van Den Broeke and Jauernic 2014; Van Den Broeke 2015). However, because of the large number of different debris types lofted in a tornado and their poorly understood scattering characteristics, determining a well-established relationship between tornado dynamics, debris, and polarimetric variables remains a challenge (Bodine et al. 2014).

A general assumption is that debris particles tumble randomly in a tornado vortex, and are expected to exhibit near-zero Z_{DR} and low ρ_{HV} values; however, TDS observations sometimes show the occurrence of negative Z_{DR} within or near a hook echo (Ryzhkov et al. 2005; Bluestein et al. 2007; Bodine et al. 2011, 2013). While it may be possible that the bias in Z_{DR} is introduced by measurement errors (errors in Z_{DR} increase as ρ_{HV} decreases; Bringi and Chandrasekar 2001), this phenomenon could also be explained by non-Rayleigh scattering, common debris alignment, Z_{DR} calibration, attenuation, or a combination of factors (Ryzhkov et al. 2005; Bluestein et al. 2007; Bodine et al. 2011, 2014).

It is reasonable to assume that debris distributions are composed of a wide range of sizes and shapes, with both

Rayleigh and non-Rayleigh scattering (Bodine et al. 2014). Non-Rayleigh scattering could cause negative Z_{DR} and low ρ_{HV} values as a result of the resonance effects that cause oscillations in the backscattered signals (Ryzhkov et al. 2005; Bodine et al. 2014). However, there are also cases where coherent negative Z_{DR} regions were observed (Bodine et al. 2011). Some studies (Bluestein et al. 2007; Bodine et al. 2011) have explored the possibility that a common alignment among debris particles may result in negative Z_{DR}. It is speculated that Z_{DR} might exhibit positive or negative values, depending on the size and mean orientation of debris, provided that there is a certain degree of common alignment. Given the large intrinsic values of Z_{DR} in debris, even a small amount of common alignment in a resolution volume could cause deviation from zero mean Z_{DR}. Furthermore, it is speculated that given the wide range of complex debris-scattering characteristics within a resolution volume, a very low ρ_{HV} value ($\rho_{HV} < 0.8$) could still be produced despite a common alignment of scatterers (Bodine et al. 2011; Griffin et al. 2017).

The main purpose of this work is to investigate the causes of nonzero mean values of Z_{DR} from a tornado dynamics perspective using a tornado and time series radar simulator (Cheong et al. 2017). In section 2 the framework and tools necessary to perform the analysis are presented. Section 3 presents the results of the orientation analysis of simulated datasets using different debris types. Conclusions and recommendations for future work are presented in section 4.

2. Methodology

a. Simulation framework

Since a definitive physical explanation for the occurrence of negative Z_{DR} signatures in tornadic observations has not yet been found, in an attempt to recreate such observations, simulations can provide a computationally constructed situation to produce realistic radar data. Hypotheses related to TDSs can be tested using combined radar and photogrammetric analyses (e.g., Wakimoto et al. 2016), and can provide insight regarding how different debris affect TDSs. A notable challenge to relating TDSs to visible debris types is that not all scatterers may be visible and the visible scatterers are assumed to be dominant. In the simulation environment, however, the characteristics of debris and their impact on the dual-polarization radar signature can be quantified directly.

SimRadar (Cheong et al. 2017) is a tool that combines a simulated tornado vortex with a polarimetric I/Q time series radar simulator; see the supplemental file JTECH-D-17-0140.s1 for an animation of SimRadar's user interface. A large-eddy simulation (LES; Maruyama 2011; Bodine et al. 2016a) is used to drive the motion and orientations of particles, along with many debris particle types of different characteristics, each with its own air drag model (ADM) to drive the trajectories, and its corresponding radar cross section (RCS) model for particle backscattering calculation. Nonspherical particle trajectories are simulated using a 6-degrees-of-freedom (6DOF) model (Maruyama and Noda 2012). At each time step, the weighted contribution of each scatterer, taking into account the RCS corresponding to the particle in its particular orientation, is summed coherently akin to the Monte Carlo integration method to produce the simulated radar data; then, the positions, velocities, orientations, and tumbling of all scatterers are updated using their corresponding LES models/ADMs.

The LES model used in the radar simulator is a turbulent three-dimensional simulation. The simulation uses axisymmetric lateral boundary conditions with a mean angular momentum of $11\,500\,m^2\,s^{-1}$. The top boundary condition is a central downdraft in the center surrounded by an annulus of updraft with a maximum updraft velocity of $22\,m\,s^{-1}$ and a maximum downdraft velocity of $20\,m\,s^{-1}$. Semislip boundary conditions with a surface roughness length of 0.1 m are used on the lower boundary condition.

Using these boundary conditions, the LES model produces a two-cell vortex structure with a central downdraft surrounded by an annulus of updraft (Fig. 2a). Axisymmetric time-averaged wind speeds are shown in Fig. 2. An intense corner flow transports angular momentum into a smaller radius compared to aloft, producing the highest mean tangential velocities exceeding $55\,m\,s^{-1}$ at 25 m AGL and a radius of 150 m. Aloft, the radius of maximum winds (RMW) expands to 250 m. Subvortices are evident in the simulation (not shown), forming along the radial gradient of tangential and vertical velocities inside the RMW, and the subvortices contribute to the maximum in turbulent kinetic energy (TKE) between 75 and 150 m (Fig. 2b). Other LES model inputs have been developed for the radar simulator to emulate different swirl ratios, diameters, etc., but the focus here is on the two-cell vortex simulation. While the simulator does not account for storm-scale physics, it provides a means to study tornado-scale dynamics around the vortex center and in some areas outside where debris centrifuging and fallout occurs.

b. Quaternions and relative quaternions

Within the simulation framework, quaternion arithmetic is used extensively in the retrieval and calculation of scatterer orientation according to ADM values, the transformation of coordinate systems (CS) to map between ADM, RCS, and radar-relative values, and for

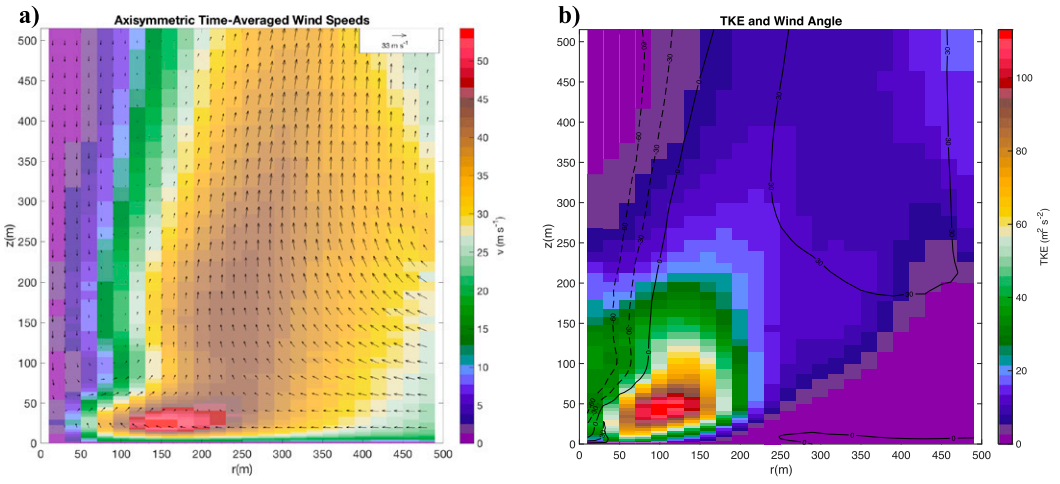

FIG. 2. Ingested LES data. (a) Axisymmetric time-averaged wind speeds, and (b) TKE and wind angle.

on-screen visualization of the simulation output. Additionally, the use of quaternions facilitates the task of extracting the orientation angles of debris relative to an absolute reference frame.

Quaternions are mathematical constructs that are essentially an extension of complex numbers. They can be represented in vector form as

$$\mathbf{q} = q_x\mathbf{i} + q_y\mathbf{j} + q_z\mathbf{k} + q_w = [q_x, q_y, q_z, q_w]. \quad (1)$$

Unit quaternions can appropriately represent the orientation of a rigid body and are not prone to gimbal lock problems as with an Euler angle representation. Furthermore, they represent spatial rotations in a more compact and less-computationally expensive way when compared to rotation matrices. A complete set of definitions and operations for quaternions can be found in Diebel (2006). All quaternions used in this work are unit quaternions unless otherwise indicated. An intuitive representation of a quaternion is with the axis-angle representation (Fig. 3a), that is, a vector given by $\hat{\mathbf{u}} = [u_x, u_y, u_z]$ and a rotation about this vector of an angle α as

$$\mathbf{q} = \left[u_x \sin\frac{\alpha}{2}, u_y \sin\frac{\alpha}{2}, u_z \sin\frac{\alpha}{2}, \cos\frac{\alpha}{2}\right]. \quad (2)$$

Any finite rotation may be achieved by a single rotation about an appropriately chosen axis (Diebel 2006). For example, the quaternion representing a composite rotation $\mathbf{q}$ about the Cartesian x, y, and z axes can be mathematically described as

$$\mathbf{q} = \mathbf{q}_{\hat{\mathbf{x}}}\mathbf{q}_{\hat{\mathbf{y}}}\mathbf{q}_{\hat{\mathbf{z}}}, \quad (3)$$

where $\mathbf{q}_{\hat{\mathbf{x}}}$, $\mathbf{q}_{\hat{\mathbf{y}}}$, and $\mathbf{q}_{\hat{\mathbf{z}}}$ represent the unit quaternions of rotation about the x, y, and z axes, respectively. A rotation of a point, or a set of points, with quaternions can be achieved through the operation

$$\mathbf{p}' = \mathbf{q}\mathbf{p}\mathbf{q}^{-1}, \quad (4)$$

where $\mathbf{p}$ denotes the four-element vector $[x, y, z, 1.0]$ (the fourth component is always set to 1.0 because they are unit quaternions) indicating the position, and $\mathbf{p}'$ is the new position postrotation.

Within the simulator different sets of orientation angles in different reference frames are used to map the appropriate ADM and RCS values to their corresponding orientation; thus, relative rotations are needed to match the proper values in the lookup tables. As shown in Fig. 3b, a world (absolute) CS ($\hat{\mathbf{x}}$, $\hat{\mathbf{y}}$, $\hat{\mathbf{z}}$) aligned with the simulation domain origin is used as a fixed reference frame for proper visualization. A debris CS ($\hat{\mathbf{x}}_D$, $\hat{\mathbf{y}}_D$, $\hat{\mathbf{z}}_D$) is selected as a convention to refer its front face, up position, and right side, respectively. It is initialized with its axes identical to the world CS, and this initial orientation is used as a reference to retrieve ADM values from a lookup table. Additionally, a radar CS ($\hat{\mathbf{x}}_R$, $\hat{\mathbf{y}}_R$, $\hat{\mathbf{z}}_R$) that moves with the radar beam for given azimuth and elevation angles is such that the local y axis is along the radar beam, the local x axis across, and the local z axis perpendicular to both. This radar-relative reference frame is used to project the objects to the radar's point of view (POV) so that the backscattering signal can be calculated correctly. Finally, an RCS reference frame ($\hat{\mathbf{x}}_{\mathrm{RCS}}$, $\hat{\mathbf{y}}_{\mathrm{RCS}}$, $\hat{\mathbf{z}}_{\mathrm{RCS}}$), similar to the radar CS but with its origin coinciding with the debris CS origin, is used to retrieve RCS values from a lookup table.

By calculating the relative change (in terms of rotation) of the CS orientation, it is possible to extract the orientation angle information that is used to map to the

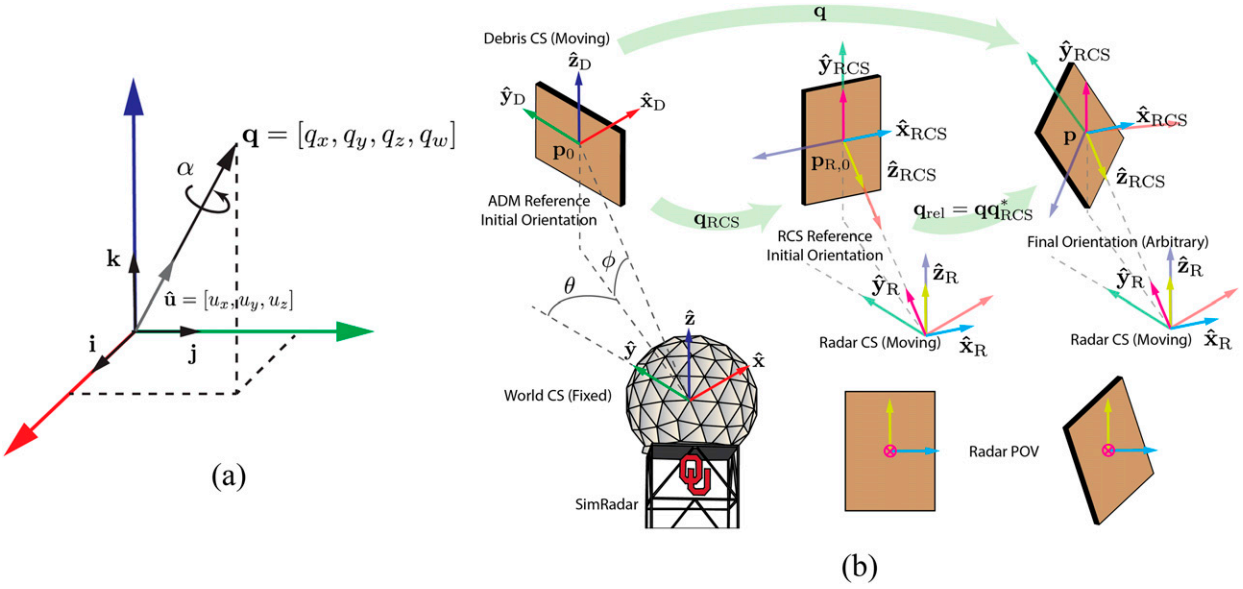

FIG. 3. (a) Axis-angle representation of a quaternion. (b) Representation of the CS used in SimRadar (Cheong et al. 2017). The debris is rotated by $\mathbf{q}$ from its initial orientation in the ADM reference frame to display the final orientation in the user interface. The quaternion $\mathbf{q}_{\text{RCS}}$ transforms the initial ADM frame orientation to the initial RCS frame orientation. The quaternion $\mathbf{q}_{\text{rel}}$ contains the information about relative changes from the final orientation referenced to the initial RCS orientation needed to map to the correct RCS value in the lookup table.

corresponding ADM and RCS values in the lookup tables. The final (absolute) orientation of an object, denoted as a group of points, is obtained by rotating its ADM-relative initial orientation by the unit quaternion $\mathbf{q}$; that is,

$$\mathbf{p} = \mathbf{q}\mathbf{p}_0\mathbf{q}^{-1} \tag{5}$$

would yield the new coordinates in the fixed reference frame, where $\mathbf{p}$ is the final position and $\mathbf{p}_0$ is the ADM-relative initial position. Thus, ADM-relative angles can be retrieved directly from $\mathbf{q}$. However, for RCS retrieval, the rotation must be relative to the initial orientation of the RCS reference frame. An intermediate step must be introduced to transform the debris CS to the RCS CS, which is done using the quaternion $\mathbf{q}_{\text{RCS}}$ (Fig. 3b). Then, a relative quaternion associated with the rotation of the RCS-relative initial orientation to the final orientation, represented by

$$\mathbf{q}_{\text{rel}} = \mathbf{q}\mathbf{q}^*_{\text{RCS}}, \tag{6}$$

is used to obtain the angles with respect to the radar CS that maps them to the appropriate values in the RCS lookup tables.

c. *Orientation angles of debris*

To extract orientation angle information from debris particles in the simulation, an absolute reference frame (such as the world CS) and a convention must be used as reference, since different rotations for different reference frames may have completely different physical interpretations. Similar to the procedure described previously to obtain the RCS-relative quaternion, an intermediate quaternion $\mathbf{q}'$ (Fig. 4) that rotates the debris from its initial orientation to a vertical orientation is used, where $\hat{\mathbf{y}}_D = \hat{\mathbf{z}}$, $\hat{\mathbf{x}}_D = -\hat{\mathbf{y}}$, and $\hat{\mathbf{z}}_D = -\hat{\mathbf{x}}$, where the subscript D is denoting debris CS. That is, the long dimension of the debris is aligned with the world z axis, while the x–z plane of the debris is aligned with the world x–y plane. In this case, the relative quaternion $\mathbf{q}_r = \mathbf{q}\mathbf{q}'^*$ contains the information about the relative changes in rotation from the vertically aligned debris to the final orientation. By using a ZYZ Euler angle convention (Diebel 2006), we can derive the orientation angles δ, ϵ, and ζ as

$$\delta = \tan^{-1}\left(\frac{q_{ry}q_{rz} + q_{rx}q_{rw}}{-q_{rx}q_{rz} + q_{ry}q_{rw}}\right), \tag{7}$$

$$\epsilon = \cos^{-1}(q_{rz}^2 + q_{rw}^2 - q_{rx}^2 - q_{ry}^2), \tag{8}$$

$$\zeta = \tan^{-1}\left(\frac{q_{ry}q_{rz} - q_{rx}q_{rw}}{q_{rx}q_{rz} + q_{ry}q_{rw}}\right). \tag{9}$$

The physical interpretation of the δ and ϵ orientation angles is the same as longitude and latitude, respectively,

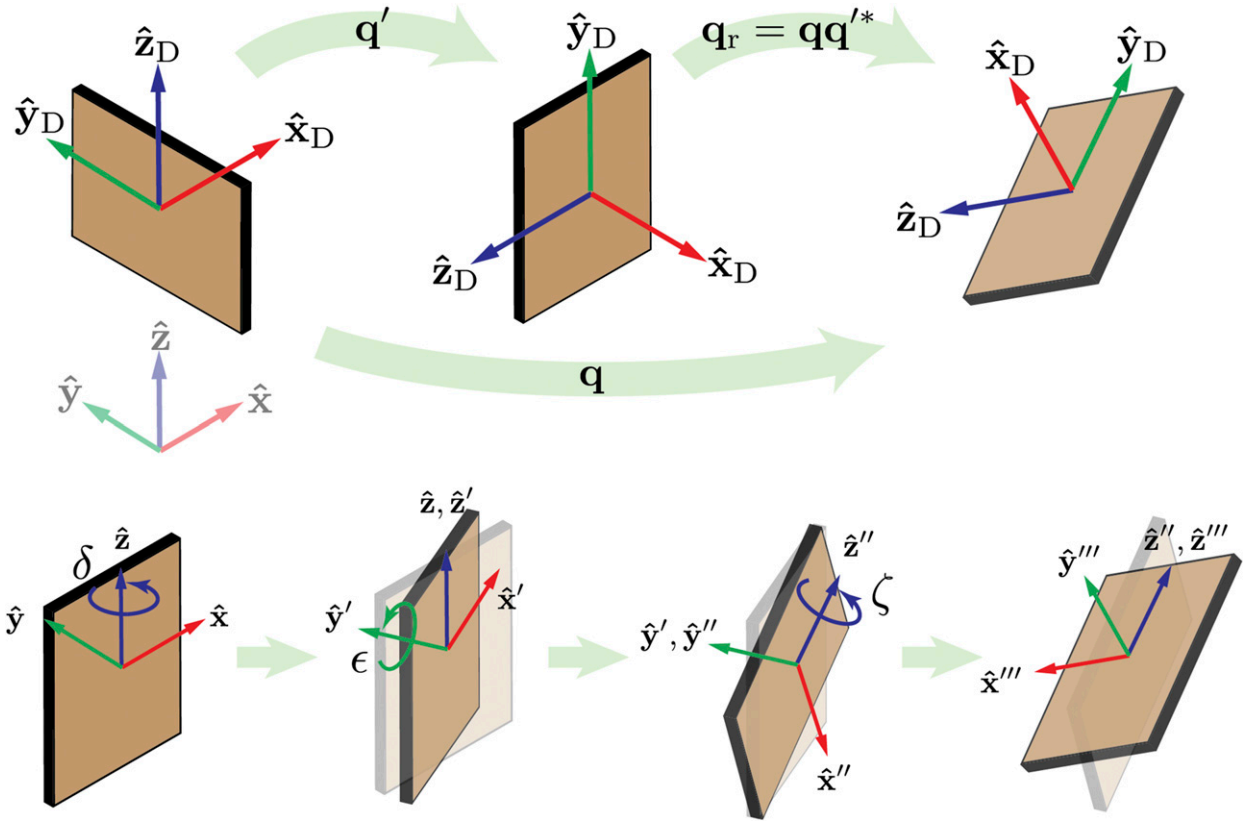

FIG. 4. Illustration of how the orientation angles are obtained. (top) The quaternion $\mathbf{q}$ rotates the debris to its final orientation. The quaternion $\mathbf{q}'$ rotates the debris to an upright orientation, and $\mathbf{q}_r$ rotates the vertically oriented debris to its final orientation. It is required to retrieve the δ, ϵ, ζ angles using the ZYZ Euler convention. (bottom) The interpretation of the angles and the convention is shown.

in a geographic coordinate system, while ζ is a rotation about the debris y axis. The analysis presented later uses this set of angles to provide a comprehensive look into the orientation angles of debris inside a tornado vortex.

Referring to Fig. 5, using a convention that x points toward east, y points toward north, and z points toward up, a set of orientation angles $\{\delta, \epsilon, \zeta\} = \{0, 0, 0\}$ would represent a vertically oriented debris element. For $\delta = \pi/2, \pi, -\pi/2$, the vertically oriented debris would have its face pointing east, north, and west, respectively. Debris with $|\epsilon| \approx 0, \pi$ represent a vertical alignment, while $|\epsilon| \approx \pi/2$ represents horizontal alignment. The physical interpretation of ζ is more challenging: for vertically aligned debris, δ and ζ are essentially rotations about the same world z axis. However, ζ acquires a more important meaning for horizontally aligned debris, where it determines whether the face is looking up/down.

d. Regions under analysis

The extent of the simulation domain encompasses a volume of approximately 800 m × 800 m × 200 m, where tornado-scale dynamics, including centrifuging and fallout, are most important. The combination of the wind-driving mechanism and the drag of the particles allows for centrifuging and fallout effects to be constructed computationally. Thus, the behavior of particles moving and tumbling differently in different regions of the vortex can be resolved.

Spatial analyses within the emulation domain can be performed in regions with different hydrometeor concentration, wind speed, and shear. Figure 6 shows an example with hydrometeors tracing (moving with) the wind, where the intensity of each pixel represents the number concentration of raindrops. Intense inflow within the corner flow region offsets the centrifugal fallout of raindrops, resulting in a clustering near the RMW.

By studying the statistics of orientation angles in smaller spatial subsets, the relationship between the wind direction and debris orientation is clearer. Given the spatial distribution of scatterers, the relative position in the vortex can be used to categorize the groups of scatterers. Three parameters of particular importance are the height (position in z), the center of the vortex,

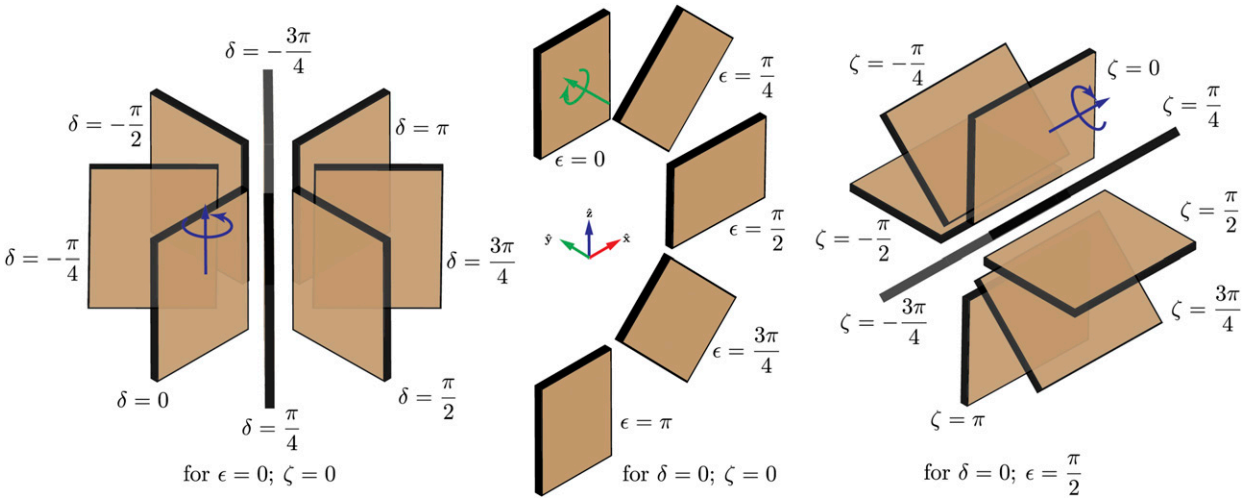

FIG. 5. Visualization of the δ, ϵ, ζ orientation angles for selected cases.

and the radius of maximum concentration of raindrops (RMC). The center of the vortex is calculated as the mean of the positions of raindrops (shown in Fig. 6b at the intersection of the grid), while the RMC is calculated with the 50% confidence interval ellipse of the positions of all raindrops (shown in Fig. 6 as an ellipse near the maximum concentration). This method is used for the purposes of this study as a quick way to obtain the center of the vortex and is not intended to be applied to radar data. The radial distance from the center of the vortex r_v is normalized, where $r_v = 1$ is at the RMC, $r_v < 1$ is within the center of the vortex, and $r_v > 1$ is outside of the center of the vortex. To identify the regions for analyses, height and radial extents will be denoted by A and B, respectively, followed by a number. Table 1 summarizes the extent of the regions, and the notations that will be used in the next section. Because of the boundary effects of the simulation and the chaotic behavior of objects close to the surface, the region below $z = 20$ m will not be included in the analysis.

3. Results

Tornadoes produce a wide range of debris types that include natural and manmade debris of various shapes and sizes (Dowell et al. 2005; WSEC 2006; Van Den Broeke 2015). The study focuses on a limited subset of three common debris types—leaves, wood boards, and metal sheets—to understand the behavior of small and large debris. The leaves were modeled as "freshly cut leaves" with a moisture content of 80%, while the properties of the wood boards and metal sheets were selected after a quick survey of typically observed values. A leaf model is chosen as a vegetation-type scatterer. The body is modeled by a rectangular plate 6 cm wide × 8 cm long, with a 0.1-cm thickness, and a density of 350 kg m^{-3}, and a stem modeled as a cylinder of 12 cm long and the same density attached to the body. A wood board is chosen as a standard wooden structural object typically found in houses. It is 10.16 cm wide × 30.48 cm long, with a 5.08-cm thickness, and a density of 500 kg m^{-3}. Finally, a square metal sheet is modeled with dimensions 100 × 100 cm^{-2}, with a 0.1-cm thickness, and a density of 7850 kg m^{-3}. The number of debris objects loaded into the simulation is 102 400 for each type. The raindrops have a Marshall–Palmer DSD with an intercept parameter of 2.3; a rain rate of 15 mm h^{-1} and five different diameter classes of 1, 2, 3, 4, and 5 mm; and the scattering amplitudes are computed using expressions from Bringi and Chandrasekar (2001). It should be noted that while the Marshall–Palmer DSD is a simple way to simulate rain DSDs, it may not be representative in many supercell situations, especially in appendage/near-tornado regions (e.g., French et al. 2015). The simulation is run with all scatterer types (raindrops and all debris types) simultaneously present. Initially, debris are populated with a random orientation and a random position in the domain, and are replaced as they fall out or exit the domain. After a spin-up time of approximately 10 min (real-time simulation), the flux of new debris becomes approximately constant, reaching a stable state. That is, the statistics observed hereafter are assumed to be reasonably time invariant.

a. *Statistical analysis of orientation angles*

1) DEPENDENCE WITH WIND DIRECTION

The relationship between the debris orientation and the wind vector sampled at the debris position is studied.

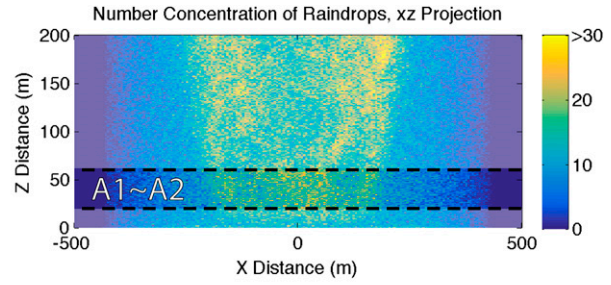

FIG. 6. (a) A 2D histogram of the concentration of raindrops projected onto the x–z plane. (b) As in (a), but for the x–y plane. The grid lines indicate the subdivision of the simulation domain in regions for the analyses, where A and B denote the height and radial extents, respectively, followed by a number indicating the extent of the region (see Table 1).

The angles between the unit vector of the wind direction $\hat{\mathbf{w}}$ and the rotated debris axes ($\hat{\mathbf{x}}'_D$, $\hat{\mathbf{y}}'_D$, $\hat{\mathbf{z}}'_D$) are obtained as

$$\gamma_x = \cos^{-1}(\hat{\mathbf{x}}'_D \cdot \hat{\mathbf{w}}), \tag{10}$$

$$\gamma_y = \cos^{-1}(\hat{\mathbf{y}}'_D \cdot \hat{\mathbf{w}}), \tag{11}$$

and

$$\gamma_z = \cos^{-1}(\hat{\mathbf{z}}'_D \cdot \hat{\mathbf{w}}). \tag{12}$$

The spatial distribution of the different debris types for the region A0–B0 is shown in Figs. 7a–c, and the histograms of the angle between the debris CS axes and the wind direction are shown in Figs. 7d–f. An important observation is that all debris types are more concentrated near the RMC in varying degrees, but the concentration of scatterers at the center of the vortex is small (Figs. 7a–c). Several works (Fujita 1981; Wakimoto and Martner 1992; Wakimoto et al. 1996; Wurman and Gill 2000; Bluestein et al. 2004; Bodine et al. 2011; Wakimoto et al. 2011; Bodine et al. 2014) have observed a reduction of Z_H within the center of the vortex, and this is a possible explanation for this phenomenon. Additionally, a decrease of Z_H as a function of height is observed (Dowell et al. 2005; Bodine et al. 2016b), which could be due to the lower concentration of debris. It is found that, on average, debris tend to have a preferred orientation for $\hat{\mathbf{x}}'_D$, such that it is aligned almost perpendicular to the wind direction (Fig. 7d). This tendency is seen for leaves with a peak around 90°, though for wood boards the distribution is more uniform for $70° < \gamma_x < 110°$, and for metal sheets the distribution is bimodal with peaks around 70° and 110°. The distribution of γ_y and γ_z for leaves shows a preferred orientation at approximately $\gamma_y = 80°$ and 110° and $\gamma_z = 150°$ and 20°. The difference of approximately 90° is expected, since the axes are orthogonal. Similarly, the wood board and the metal sheet also show a bimodal tendency; however, it is much less pronounced, presumably because of the difference in aerodynamic characteristics of the objects. A physical interpretation for this is that, for example, leaves will tend to move with the wind with $\hat{\mathbf{y}}_D$, $\hat{\mathbf{z}}_D$ almost perpendicular to the direction of the wind and with minor tumbling. While the peaks in γ_y and γ_z for wood boards and metal sheets suggest that a small degree of alignment with the wind may be possible, the more uniform distribution of angles in these objects indicate that they predominantly experience more tumbling than leaves, which may be owed to the difference in drag characteristics and a larger moment of inertia.

To summarize, the debris orientation is dependent on the wind force impinged upon it, and leaves show common alignment in horizontal axes. While this confirmation might not be unexpected, it serves as a "soft" validation that the wind fields can, in fact, cause light

TABLE 1. Extent of the regions under analysis for different heights (z) and radial distances (r_v).

Region	Extent
A0	$z \geq 20$ m
A1	$20 < z \leq 40$ m
A2	$40 < z \leq 60$ m
A3	$60 < z \leq 80$ m
A4	$80 < z \leq 100$ m
A5	$z > 100$ m
B0	$r_v > 0$
B1	$0 < r_v \leq 0.8$
B2	$0.8 < r_v \leq 1.2$
B3	$r_v > 1.2$

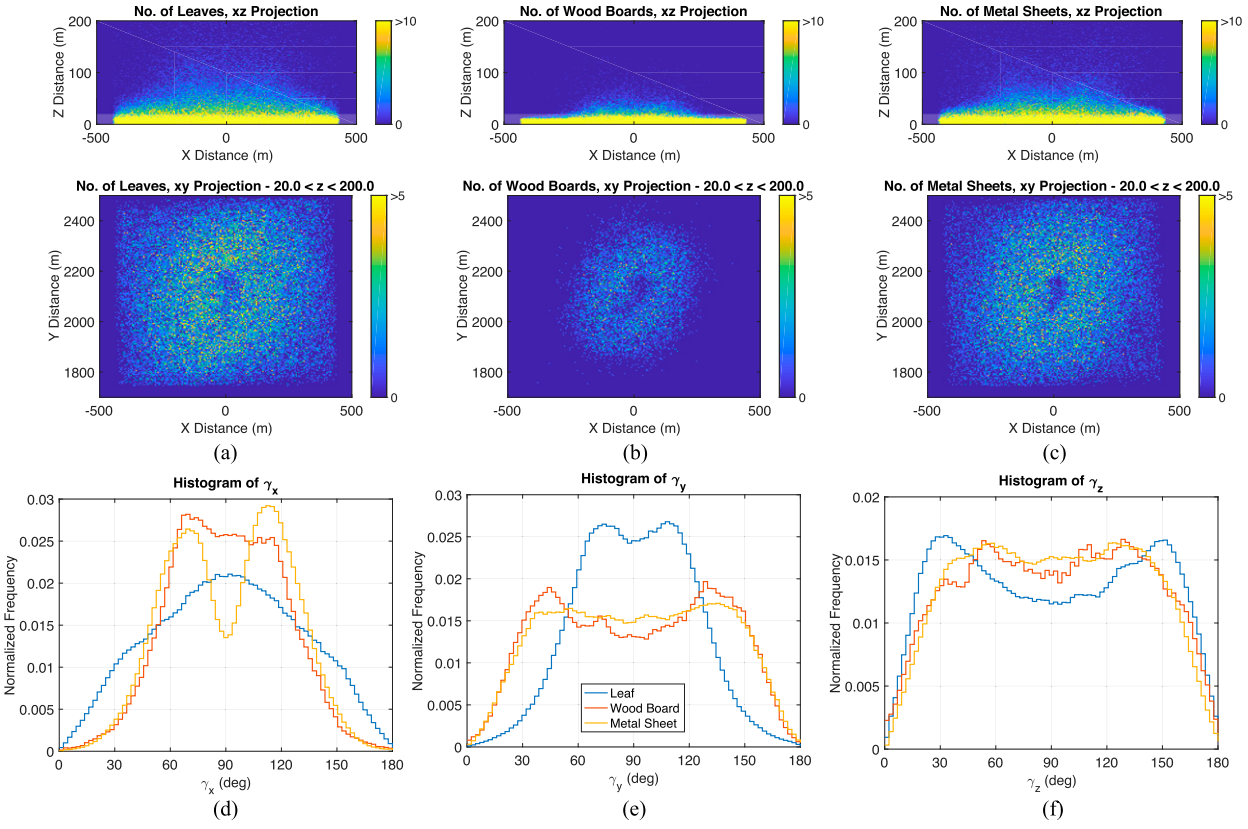

FIG. 7. (a) A 2D histogram of the concentration of leaves projected onto the (top) x–z plane and (bottom) x–y plane for A0–B0. (b) As in (a), but for wood boards. (c) As in (a), but for metal sheets. (d)–(f) Histograms of the angle between $\hat{\mathbf{x}}'_D$, $\hat{\mathbf{y}}'_D$, $\hat{\mathbf{z}}'_D$ and $\hat{\mathbf{w}}$, γ_x, γ_y, γ_z, respectively, for different debris types.

debris to have a common alignment that depends on the driving wind force.

2) DEPENDENCE WITH HEIGHT

To study the height dependence of the δ, ϵ, ζ angles, the regions A1–A5 with B0 fixed (i.e., different heights for all radial distances; see Table 1) will be analyzed. Figure 8 shows the histograms of δ, ϵ, and ζ for leaves, wood boards, and metal sheets at different heights. As expected, the δ angle (which represents the longitude; i.e., the direction the debris is facing parallel to the x–y plane) for all debris types is uniformly distributed when the regions under analysis are volume slices limited by height. Moreover, the ζ (which represents a rotation about the debris y axis) distribution for all debris types agrees with the result from the previous section, where the $\hat{\mathbf{x}}_D$ axis tended to be aligned perpendicularly (i.e., peaks around $-90°$ and 90°) with the direction of the wind (Figs. 8c,f,i), and with peaks around $\pm 120°$ for larger debris, likely resulting from differences in inertial and aerodynamic characteristics. An interpretation of this is that the δ angle will align the debris CS with the wind, while the ζ angle will align it perpendicularly, that is, aligning it with the face pointing up/down parallel with vertical drag.

On the other hand, differences can be observed in the distributions of ϵ and ζ (Figs. 8b,c,e,f,h,i). Leaves (Figs. 8a–c) exhibit a bimodal distribution in ϵ (which represents the latitude; i.e., the debris canting angle), and this trend becomes more prominent at greater heights. In other words, they show a preferred orientation of the canting angle that is increasingly more vertical with height. Wood boards are mostly confined to the lowest heights of the volume and the number of particles that match the threshold imposed by height is increasingly lower. Thus, the histograms have fewer data points at greater heights and they appear to be noisier. Nonetheless, a somewhat similar behavior is observed, with a preferred slightly less horizontal orientation with peaks at 65° and 115° at lower heights (blue line, Fig. 8e). The flatter distribution of ϵ suggests wood boards are tumbling more than leaves. The ζ distribution deviates slightly from

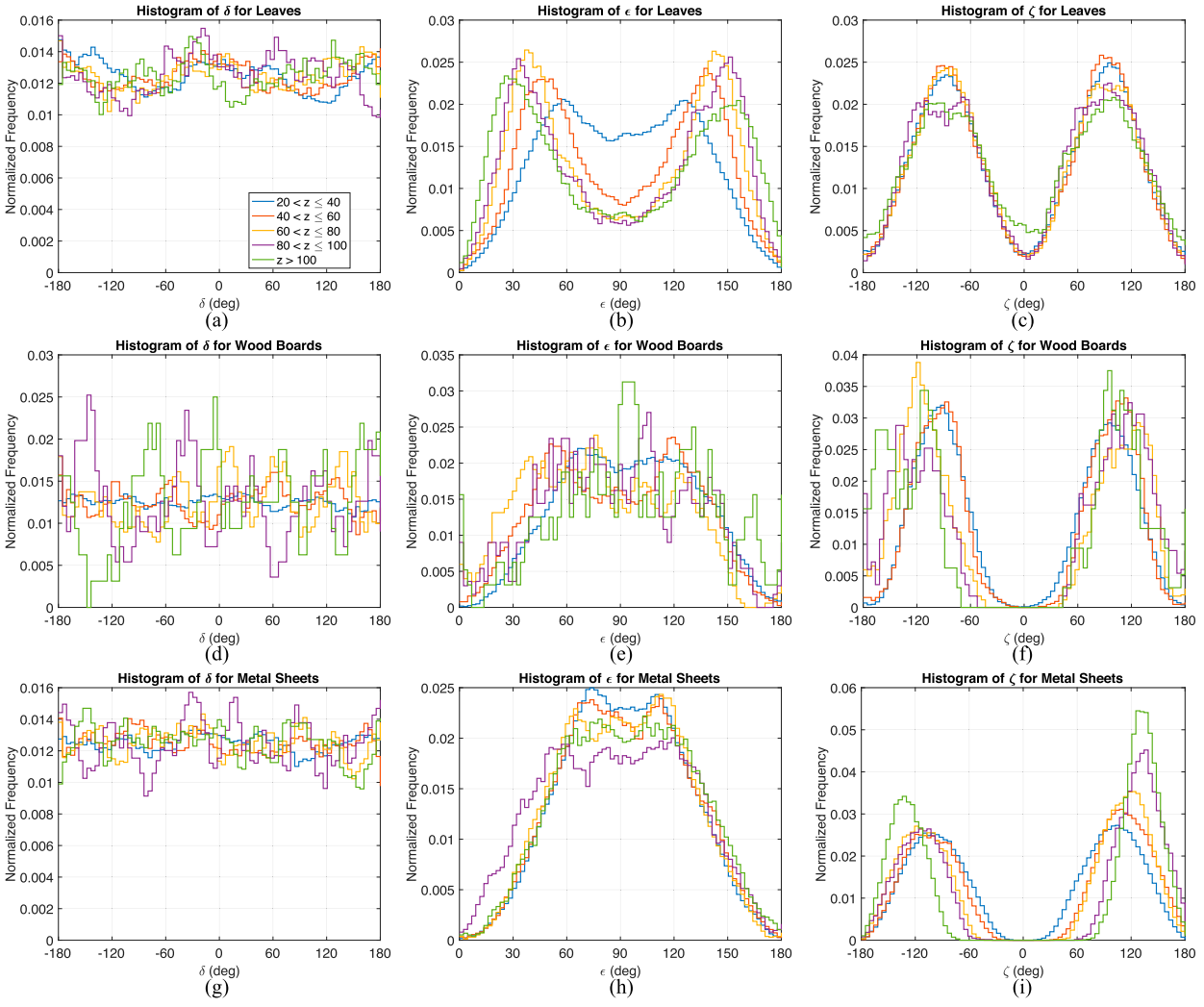

FIG. 8. (a)–(c) Histograms of δ, ϵ, ζ, respectively, for leaves at different heights. (d)–(f) As in (a)–(c), respectively, but for wood boards. (g)–(i) As in (a)–(c), respectively, but for metal sheets.

the peaks at −115° and 90°, presumably because of their rotational inertia. Similar conclusions can be made about the distribution of angles in metal sheets; however, the canting angles are more centered about a horizontal orientation than with the leaves and wood boards.

A physical explanation is that at low levels random initial orientations of debris lead to flatter distributions. Moreover, higher turbulence, evident by higher TKE below 50 m in Fig. 2a, may contribute to the flatter distributions. The wind angle, defined as the angle of the wind vector off the horizontal plane, is shown in Fig. 2b. In the center of the tornado, where the central downdraft is present and tangential velocities are weak, debris are aligned more horizontally consistent with large, negative wind angles. At larger radii aloft, the wind angle has a small positive value and reflects a greater contribution of tangential motion compared to vertical motion. In this region the debris tend to be more vertically aligned. In summary, the most common debris orientation is for the largest face of the debris to be oriented normal to the wind angle, in a position where drag forces acting on the debris are higher.

Bodine et al. (2014) observed that Z_{DR} became more negative with height. They speculated that this result could arise from a greater tendency of smaller, less-dense debris to exhibit a greater degree of common alignment, whereas larger debris near the surface exhibit a lower degree of common alignment. The results of this analysis agree with that hypothesis, particularly with leaves exhibiting more common alignment

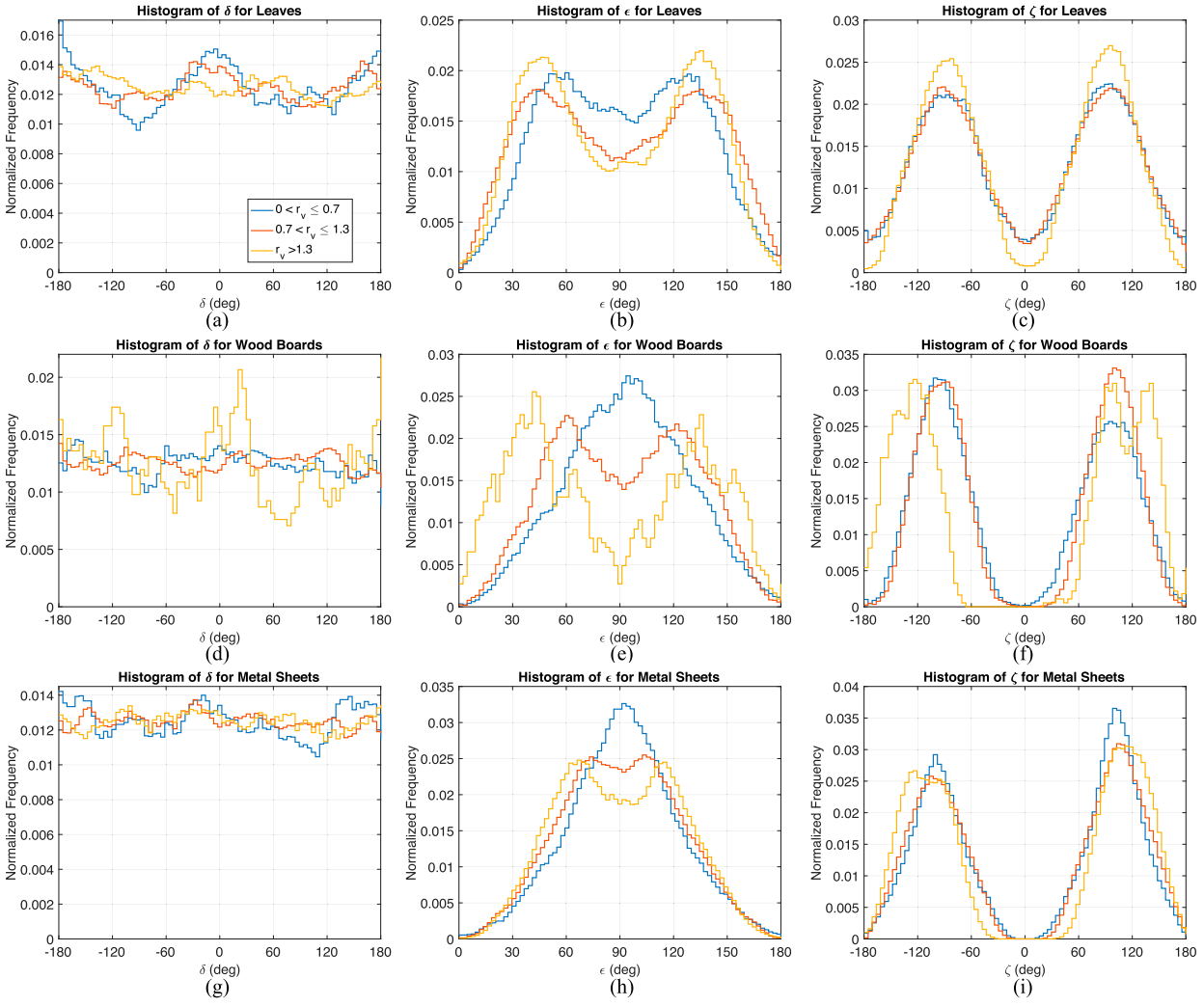

FIG. 9. (a)–(c) Histograms of δ, ϵ, ζ, respectively, for leaves at different radial distances. (d)–(f) As in (a)–(c), respectively, but for wood boards. (g)–(i) As in (a)–(c), respectively, but for metal sheets.

than heavier debris and two out of three debris species becoming more vertically aligned with height.

3) DEPENDENCE WITH RADIUS

This analysis corresponds to elliptical regions for all heights, denoted B1–B3, while A0 is fixed, that is, the regions inside the center of the vortex, around the RMC, and outside of the center of the vortex. Figure 9 shows the histograms of the δ, ϵ, and ζ angles of leaves, wood boards, and metal sheets for different radial distances. The δ and ζ angles do not exhibit many differences from our previous analysis of height dependence. However, noticeable differences are shown in the distribution of ϵ angles (Figs. 9b,e,h). The distributions of ϵ for leaves show peaks at around $45°, 135°$ for $r_v \geq 0.8$, and at $60°, 130°$ within $r_v < 0.8$. While the mean angle does not vary much as a function of the radial distance from the center of the vortex, the occurrence of these preferred orientations is higher for larger radii. On the other hand, the distribution of ϵ for wood boards shows a striking difference for the three different regions. The wood boards within the center of the vortex are oriented mostly horizontally, while they become more vertically oriented as the distance from the vortex center increases (Fig. 9e). This is consistent with the physical explanation given in the previous analysis: for weak tangential velocities and strong central downdraft, debris are more horizontally aligned with negative wind angles; for stronger tangential velocities and smaller wind angles, debris are more vertically aligned. A similar distribution is observed for metal sheets, though it is less accentuated (Fig. 9h). To summarize the observations and the

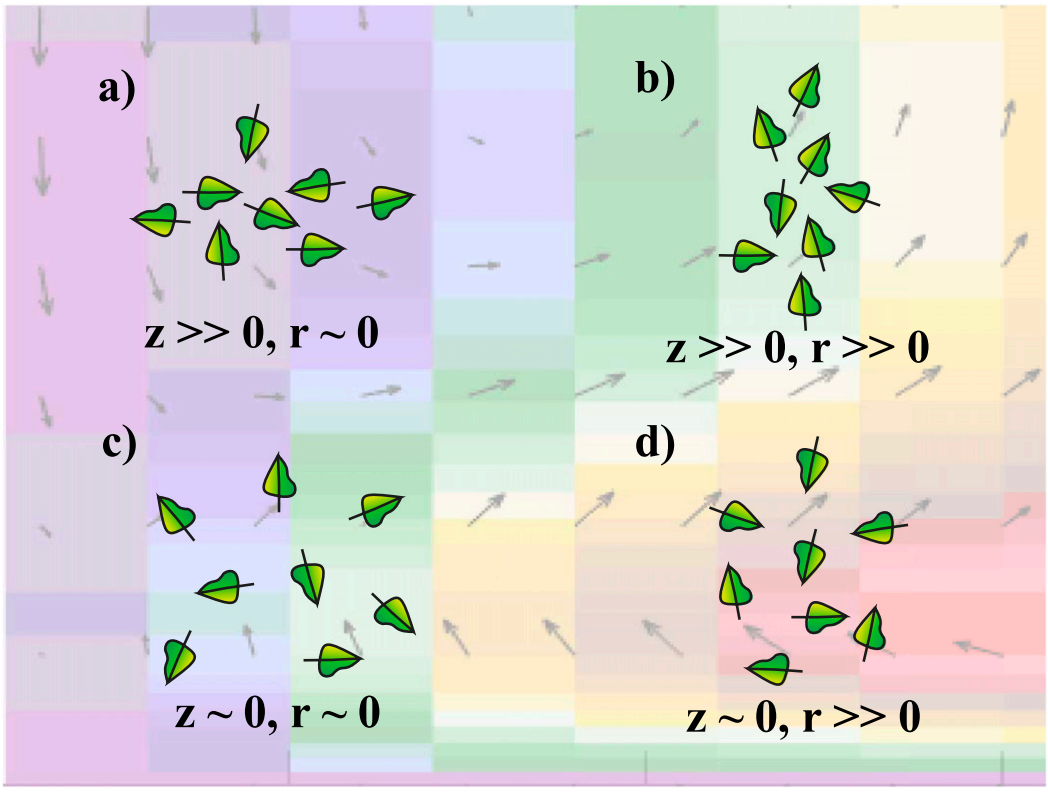

FIG. 10. Illustration of the orientation of debris for different heights and radii with the axisymmetric time-averaged wind fields in the background. (a) Closer to the center and aloft, debris tend to be more horizontally oriented. (b) Aloft and for greater radii, debris tend to be more vertically oriented. (c) Closer to the ground and to the center, debris tend to be randomly oriented. (d) Closer to the ground and for greater radii, debris show a less prominent preferred orientation.

physical explanation, a representation of the orientation of leaves for different heights and radii is presented in Fig. 10. Aloft and closer to the center, debris tend to be more horizontally oriented (Fig. 10a), while aloft and for greater radii, debris tend to be more vertically oriented (Fig. 10b). Closer to the ground and to the center, the orientation angles show a random distribution (Fig. 10c), and closer to the ground and for greater radii, debris show a less prominent preferred orientation (Fig. 10d).

This analysis suggests that a common alignment could exist in certain regions of the tornado, which could result in negative Z_{DR} because of the distribution of ϵ indicating a vertical alignment of debris particles. Griffin et al. (2017) found negative Z_{DR} at the periphery of large tornado subvortices and on the end of the TDS, which agrees with this finding. Additionally, it is speculated that the decreasing concentration of debris near the center of the vortex, in combination with a predominantly horizontal orientation for debris with higher returns (i.e., wood boards and metal sheets), could be a plausible explanation for higher ρ_{HV} values near the center of the vortex, as observed by Bodine et al. (2014), resulting from the higher homogeneity of the returned signals, and the relatively larger backscatter from rain in the center.

b. *Simulated radar observations*

In addition to studying the statistics of orientation angles, it is of particular interest to find out whether the debris objects are, in fact, able to produce TDSs in simulated data. A plan position indicator (PPI) and spectral analyses of the simulated radar signals are presented next for three cases: weather only, debris only, and weather and debris. The radar parameters (Table 2) are similar to typical WSR-88D values, though the pulse repetition time (PRT) is arbitrarily modified to ensure there is no velocity aliasing, and the range sampling is 30 m with a gate spacing of 15 m. The small resolution volume size used may result in radar signatures being observed that would not be observed by a typical NEXRAD, but these signatures might be seen with mobile radars. The domain is populated with 1.024×10^6 scatterers with five different diameter

TABLE 2. Radar acquisition and simulation domain parameters.

Radar parameters	
PRT	0.2 ms
Wavelength	10 cm
Peak transmit power	50 kW
Transmit pulse width	0.2 μs
Antenna gain	50 dB*i*
Antenna beamwidth	1.0°
Range resolution	30 m
Gate spacing	15 m
Samples per dwell	100
Azimuthal sampling	0.5°
Max unambiguous velocity	82.5 m s^{-1}
Simulation domain	
Scatterer type	Raindrop
No. of scatterers	1.024×10^6
DSD	Marshall–Palmer
Intercept parameter	2.3
Rain rate	15 mm h^{-1}
No. of diameter classes	5 (1, 2, 3, 4, 5 mm)
Scatterer type	Leaf
No. of scatterers	1.024×10^6
Dimensions (body)	6 cm wide × 8 cm long, with 0.1-cm thickness
Dimensions (stem)	12 cm long
Density	350 kg m^{-3}
LES model	Two-cell vortex
Size of simulation domain	864.77 m × 738.81 m × 217.02 m

classes of 1, 2, 3, 4, and 5 mm, for a rain rate of 15 mm h^{-1} with an intercept parameter of 2.3 for the weather-only case, and 1.024×10^6 leaves for the debris-only case. In both cases there are about 240 scatterers per cell, which satisfies the recommended scatterer density in Cheong et al. (2017). For the scenario with weather and debris, the domain is populated with a count of 1.024×10^6 raindrops and 1.024×10^6 leaves, for a total of 2.048×10^6 particles with a density of approximately 470 particles per cell, and with the same radar acquisition parameters. The rest of the simulation parameters are listed in Table 2.

The PPI plots of the signal-to-noise ratio (SNR), mean radial velocity $\overline{v}_r$, Z_{DR}, and ρ_{HV} for the simulated cases are shown in Fig. 11. The SNR is defined as SNR = S/N, with $S = R - N$, where R is the total received power, S is the signal power, and N is the noise power. It is preferred over Z_H or R_H, since it is not weighted by range and is independent of noise levels, which is especially helpful in spectral analysis when discriminating signals from different sources. As expected, the weather-only case (Fig. 11a) shows a ringlike structure in the SNR field and a strong vortex in the velocity field. Also, the Z_{DR} field shows that moderately sized raindrops with a Z_{DR} of approximately 2 dB are moving at a distance of approximately 200 m from the vortex center and with smaller-sized raindrops in the center of the vortex, resembling what appears to be a ring in the SNR and Z_{DR} fields. The ρ_{HV} is also consistently high, as expected, since the simulation domain is populated only with raindrops. A more interesting case is the one with the debris signals only (Fig. 11b), where a ring of high SNR and negative Z_{DR} can be appreciated in the SNR and Z_{DR} fields, while ρ_{HV} exhibits a region with low values collocated with the center of the tornado vortex. The low-to-negative values of Z_{DR} could be attributed to a common alignment of the leaves, which is supported by the high ρ_{HV} in the annular region (i.e., common alignment results in more homogeneous scattering). In the weather-and-debris case (Fig. 11c), the signature in the PPIs looks similar to a TDS. It is important to note that TDS-like signatures are not produced *unless* there is a rain-and-debris mix in the simulation. The signal returned from only debris is relatively homogeneous, evidenced by the high ρ_{HV} values (Fig. 11b, bottom right), and when the two signals are combined, the loss in homogeneity results in a signature that is similar to a TDS. Wakimoto et al. (2015) found a ring of low ρ_{HV} in X-band data with embedded regions of high ρ_{HV}, similar to the signature seen here. The opposite of this pattern (high ρ_{HV} in the center and a ring of low ρ_{HV} surrounding it) was observed by Bodine et al. (2014) and Houser et al. (2016). Only a few studies have used high-resolution polarimetric data to look at 3D TDS structure, so the fact that a ring does appear in the small sample size of observations suggests that while the simulator is somewhat idealized, it can represent unique structures within TDS.

Since it is possible to analyze each signal and the composite signal separately, spectral analysis may provide additional information on the interaction between hydrometeors and debris. For this, the dual-polarization spectral densities (DPSD) are calculated using the bootstrap estimator described in Umeyama et al. (2017). The DPSD depict the distribution of the polarimetric variables as a function of their Doppler velocity for a given radar resolution volume. Key DPSD of a ray corresponding to an azimuth of $\theta = 0.5°$ are presented in Fig. 12. The range–Doppler plots of the weather-only case show unimodal weather spectra for most parts of the domain. Additionally, some signatures of possible size sorting as a result of the drag forces can be observed as larger drops (larger sZ_{DR}) are collocated with smaller radial velocities than smaller raindrops (smaller sZ_{DR}), for example, from 1.85 to 1.9 km, and from 2.35 to 2.4 km (see annotations in Fig. 12a, sZ_{DR}). The correlation coefficient indicates high values owing to the homogeneity of the scatterers in motion and small backscattered differential phases.

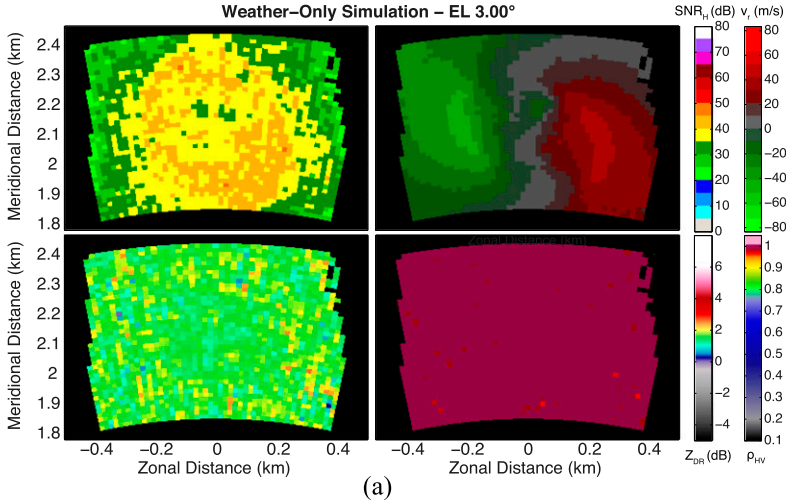

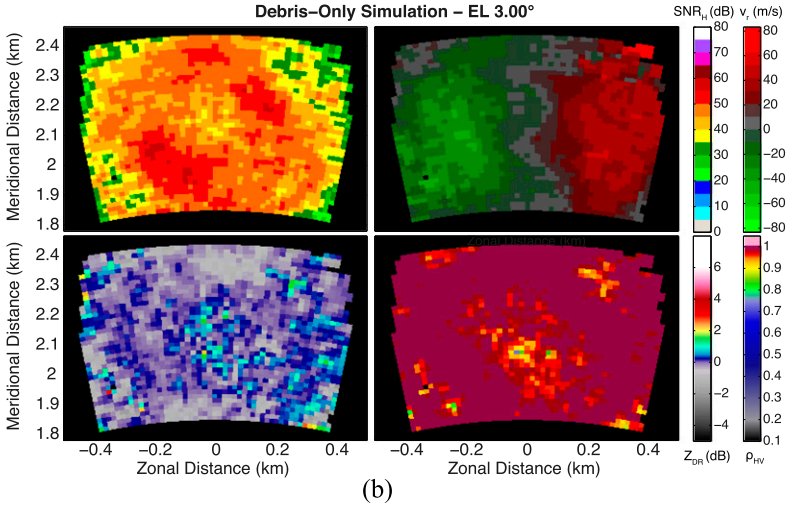

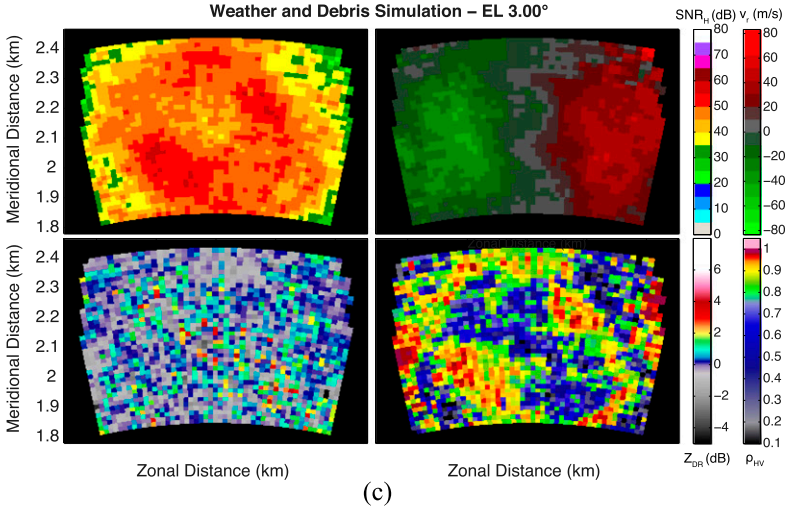

FIG. 11. PPI fields of simulated data at an elevation $\phi = 3.00°$, approximately 100 m above radar level: (top left) $\mathrm{SNR_H}$, (top right) $\overline{v}_r$, (bottom left) Z_{DR}, and (bottom right) ρ_{HV} for (a) weather-only, (b) debris-only, and (c) weather-and-debris cases.

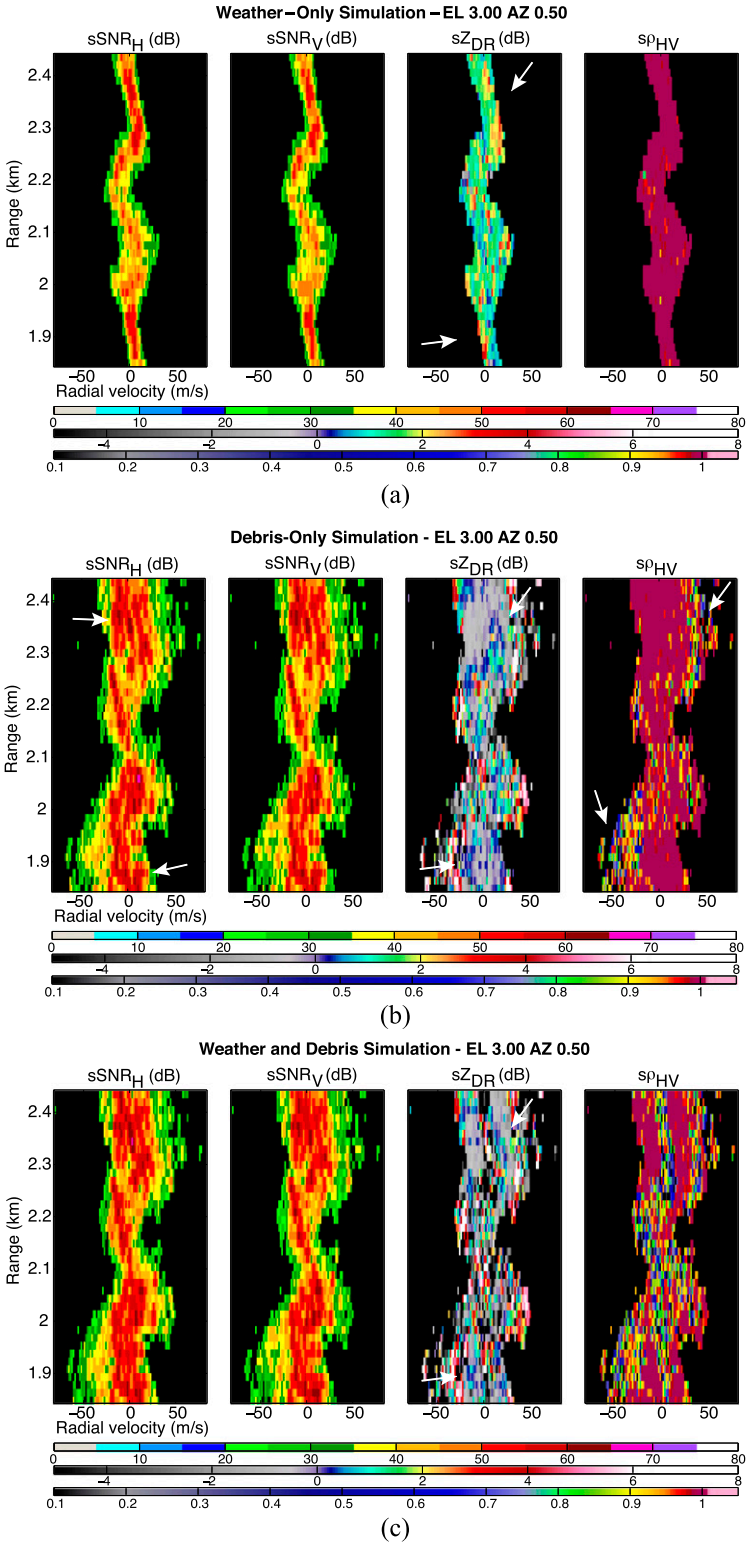

FIG. 12. Range–Doppler plots of DPSD estimates for the simulated data in Fig. 11 at $\phi = 3.00°$ and $\theta = 0.5°$ for (a) weather-only, (b) debris-only, and (c) weather-and-debris cases. The annotations in (a) indicate possible signatures of size sorting (large sZ_{DR}) and in (b) signatures with mean radial velocities close to zero and with low $s\rho_{HV}$ values.

The range–Doppler plots of the debris-only case show multimodal spectra in SNR, as well as a wide range of sZ_{DR} values, while the $s\rho_{HV}$ suggests centrifuging of debris (Fig. 12b). With the radar beam pointing approximately perpendicular to the vortex-relative wind direction, a reasonable assumption is that most leaves that are carried by the wind will have a mean radial velocity close to zero with a small deviation caused by the flow into/out of the tornado. This observation is clear between ranges 1.85 and 2.05 km, and between 2.25 and 2.4 km (see annotations in Fig. 12b, $s\text{SNR}_H$). Additionally, the high $s\rho_{HV}$ values collocated with the mean radial velocities suggest higher homogeneity of the scatterers, which is known to be true in this simulation setup. Finally, another interesting signature observed in these plots is how a few of the nondominant peaks in the spectra exhibit higher motion toward (away from) the radar for the southern (northern) region of the vortex, as if these debris were being ejected radially outward from the center of the vortex. They are also collocated with low $s\rho_{HV}$ values, suggesting these leaves may be tumbling wildly and not commonly aligned with the wind flow (see annotations in Fig. 12b, $s\rho_{HV}$). Additionally, we note that larger debris tend to have nonzero radial velocities at ranges where wind is largely perpendicular to the radar beam.

Upon closer inspection of the PPIs, and by comparing the radial velocity fields, it can be observed in the northwestern quadrant that the wind motion seems to be underestimated, while it is overestimated at the northeastern quadrant. Spectral analysis of the mixed weather and debris case shows that the spectra are mostly dominated by debris (Fig. 12c), as the signatures in SNR are very similar to those of the debris-only case (Fig. 12b). Clearly, the biases in the mean radial velocities are due to the high-power returns from debris. However, even when the weather signal is dominated to some degree by debris, certain signatures can be observed in the spectral correlation coefficient. Depending on the difference in power of the signals that are mixed in the composite signal, certain features remain identifiable. By comparing the range–Doppler plots of the three cases, it is evident that a line of low $s\rho_{HV}$ is embedded in the weather-and-debris spectral signature, and it is collocated mostly with the peak of the weather spectral signature (Fig. 12). Additionally, the decrease in $s\rho_{HV}$ can be attributed to the individual signals being relatively close to each other in SNR (i.e., within 20 dB of each other), such that none of them are dominant in that particular spectral coefficient, hence decreasing the homogeneity of the scattered signal; that is, the lower $s\rho_{HV}$ is where rain and debris coexist. Finally, it is worth noting that in a true tornado with radar observations, there will be differences in velocities based on the direction the tornado is moving, and the combination of debris-caused bias and translational velocity can make for potentially large disparities from the ideal vortex in real-world data.

4. Conclusions

The goal of this study was to investigate the cause of nonzero mean values of Z_{DR} through a statistical analysis of the spatial distribution of simulated debris orientation data, and to provide plausible explanations for additional hypotheses regarding tornado and debris dynamics derived from real observations while showcasing the SimRadar (Cheong et al. 2017) simulator as a powerful tool to study the behavior of raindrops and debris in realistic tornadic environments. Three debris types—that is, leaves, wood boards, and metal sheets—were selected because of their inherently different electromagnetic and aerodynamic characteristics, and because they are representative examples of airborne tornadic debris. When analyzing debris orientation compared to the impinging wind force, it was found that leaves tend to show common horizontal alignment with the wind and less tumbling, whereas wood boards and metal sheets showed a small degree of alignment and more tumbling because of larger moments of inertia and different drag characteristics. All debris types had a smaller concentration at the center of the vortex, which may explain the reduction of Z_H observed by Fujita (1981), Wakimoto and Martner (1992), Wakimoto et al. (1996), Wurman and Gill (2000), Bluestein et al. (2004), Bodine et al. (2011), Wakimoto et al. (2011), and Bodine et al. (2014). Concentrations of lighter and/or more aerodynamic debris tend to decrease rapidly as a function of height, which could serve as an explanation for lower Z_H with increasing height as observed by Dowell et al. (2005) and Bodine et al. (2016b). Additionally, the distributions of debris orientations classified by height showed that two out of three debris types (leaves and wood boards) tend to become increasingly vertically aligned at greater heights, which is a potential explanation for Z_{DR} becoming more negative with height as observed by Bodine et al. (2014). Heavier objects (i.e., wood boards and metal sheets) showed a decreased concentration near the center of the vortex, in addition to a strong dependence of the canting angle with the radial distance relative to the center of the vortex; that is, they showed a vertical alignment at the periphery of the tornado vortex and a horizontal alignment at the center. This agrees with the findings of Griffin et al. (2017), and it may explain higher ρ_{HV} values near the center as observed by Bodine et al. (2014). The 6DOF model shows that for both small and large platelike debris, the debris face tends to have some

common degree of alignment normal to the wind direction. Furthermore, PPI plots from simulated data showed that signatures similar to observed TDS may be obtained, provided a mixture of hydrometeors and debris is present in the domain, and that polarimetric spectral analysis on TDS may provide more information for discriminating and separating weather and debris signatures (e.g., for debris centrifuging correction).

Future work includes providing answers to several scientific questions, which include studying the behavior of ρ_{HV} and other polarimetric variables for different debris types and sizes, and the dependence on TDS size and tornado dynamics; the next immediate step is to expand the library of debris objects that can be ingested into the simulator and the application of polarimetric spectral densities to correct velocity bias.

Acknowledgments. This work was supported by the National Science Foundation under Research Grant AGS-1303685. The authors acknowledge T. Maruyama for the collaboration and for providing LES model code and wind tunnel measurements for ADM. Additional thanks to R. Palmer and C. Griffin for providing useful comments, which helped to improve the paper.

REFERENCES

Bluestein, H. B., C. C. Weiss, and A. L. Pazmany, 2004: The vertical structure of a tornado near Happy, Texas, on 5 May 2002: High-resolution, mobile, W-band, Doppler radar observations. *Mon. Wea. Rev.*, **132**, 2325–2337, https://doi.org/10.1175/1520-0493(2004)132<2325:TVSOAT>2.0.CO;2.

——, M. M. French, R. L. Tanamachi, S. J. Frasier, K. Hardwick, F. Junyent, and A. L. Pazmany, 2007: Close-range observations of tornadoes in supercells made with a dual-polarization, X-band, mobile Doppler radar. *Mon. Wea. Rev.*, **135**, 1522–1543, https://doi.org/10.1175/MWR3349.1.

Bodine, D. J., M. R. Kumjian, A. J. Smith, R. D. Palmer, A. V. Ryzhkov, and P. L. Heinselman, 2011: High-resolution polarimetric observations of an EF4 tornado on 10 May 2010 from OU-PRIME. *35th Conf. on Radar Meteorology*, Pittsburgh, PA, Amer. Meteor. Soc., 4B.3, https://ams.confex.com/ams/35Radar/webprogram/Paper191661.html.

——, ——, R. D. Palmer, P. L. Heinselman, and A. V. Ryzhkov, 2013: Tornado damage estimation using polarimetric radar. *Wea. Forecasting*, **28**, 139–158, https://doi.org/10.1175/WAF-D-11-00158.1.

——, R. D. Palmer, and G. Zhang, 2014: Dual-wavelength polarimetric radar analyses of tornadic debris signatures. *J. Appl. Meteor. Climatol.*, **53**, 242–261, https://doi.org/10.1175/JAMC-D-13-0189.1.

——, T. Maruyama, R. D. Palmer, C. J. Fulton, H. B. Bluestein, and D. C. Lewellen, 2016a: Sensitivity of tornado dynamics to soil debris loading. *J. Atmos. Sci.*, **73**, 2783–2801, https://doi.org/10.1175/JAS-D-15-0188.1.

——, R. D. Palmer, T. Maruyama, C. J. Fulton, Y. Zhu, and B. L. Cheong, 2016b: Simulated frequency dependence of radar observations of tornadoes. *J. Atmos. Oceanic Technol.*, **33**, 1825–1842, https://doi.org/10.1175/JTECH-D-15-0120.1.

Bringi, V. N., and V. Chandrasekar, 2001: *Polarimetric Doppler Weather Radar: Principles and Applications.* Cambridge University Press, 636 pp.

Bunkers, M. J., and M. A. Baxter, 2011: Radar tornadic debris signatures on 27 April 2011. *Electron. J. Oper. Meteor.*, **12** (7), 1–6.

Cheong, B. L., D. J. Bodine, C. J. Fulton, S. M. Torres, T. Maruyama, and R. D. Palmer, 2017: SimRadar: A polarimetric radar time-series simulator for tornadic debris studies. *IEEE Trans. Geosci. Remote Sens.*, **55**, 2858–2870, https://doi.org/10.1109/TGRS.2017.2655363.

Diebel, J., 2006: Representing attitude: Euler angles, unit quaternions, and rotation vectors. Stanford University Doc., 35 pp., https://www.swarthmore.edu/NatSci/mzucker1/papers/diebel2006attitude.pdf.

Dowell, D. C., C. R. Alexander, J. M. Wurman, and L. J. Wicker, 2005: Centrifuging of hydrometeors and debris in tornadoes: Radar-reflectivity patterns and wind-measurement errors. *Mon. Wea. Rev.*, **133**, 1501–1524, https://doi.org/10.1175/MWR2934.1.

French, M. M., D. W. Burgess, and E. R. Mansell, 2015: Bulk hook echo raindrop sizes retrieved using mobile, polarimetric Doppler radar observations. *J. Appl. Meteor. Climatol.*, **54**, 423–450, https://doi.org/10.1175/JAMC-D-14-0171.1.

Fujita, T. T., 1981: Tornadoes and downbursts in the context of generalized planetary scales. *J. Atmos. Sci.*, **38**, 1511–1534, https://doi.org/10.1175/1520-0469(1981)038<1511:TADITC>2.0.CO;2.

Griffin, C. B., D. J. Bodine, and R. D. Palmer, 2017: Kinematic and polarimetric radar observations of the 10 May 2010, Moore–Choctaw, Oklahoma, tornadic debris signature. *Mon. Wea. Rev.*, **145**, 2723–2741, https://doi.org/10.1175/MWR-D-16-0344.1.

Houser, J. L., H. B. Bluestein, and J. C. Snyder, 2016: A finescale radar examination of the tornadic debris signature and weak-echo reflectivity band associated with a large, violent tornado. *Mon. Wea. Rev.*, **144**, 4101–4130, https://doi.org/10.1175/MWR-D-15-0408.1.

Kumjian, M. R., and A. V. Ryzhkov, 2008: Polarimetric signatures in supercell thunderstorms. *J. Appl. Meteor. Climatol.*, **47**, 1940–1961, https://doi.org/10.1175/2007JAMC1874.1.

Maruyama, T., 2011: Simulation of flying debris using a numerically generated tornado-like vortex. *J. Wind Eng. Ind. Aerodyn.*, **99**, 249–256, https://doi.org/10.1016/j.jweia.2011.01.016.

——, and M. Noda, 2012: Tornado-borne debris. *J. Wind Eng.*, **37**, 124–129, https://doi.org/10.5359/jawe.37.124.

Palmer, R. D., and Coauthors, 2011: Observations of the 10 May 2010 tornado outbreak using OU-PRIME: Potential for new science with high-resolution polarimetric radar. *Bull. Amer. Meteor. Soc.*, **92**, 871–891, https://doi.org/10.1175/2011BAMS3125.1.

Ryzhkov, A. V., T. J. Schuur, D. W. Burgess, and D. S. Zrnić, 2005: Polarimetric tornado detection. *J. Appl. Meteor.*, **44**, 557–570, https://doi.org/10.1175/JAM2235.1.

Scharfenberg, K. A., and Coauthors, 2005: The Joint Polarization Experiment: Polarimetric radar in forecasting and warning decision making. *Wea. Forecasting*, **20**, 775–788, https://doi.org/10.1175/WAF881.1.

Schultz, C. J., and Coauthors, 2012a: Dual-polarization tornadic debris signatures Part I: Examples and utility in an operational setting. *Electron. J. Oper. Meteor.*, **13**, 120–137.

——, and Coauthors, 2012b: Dual-polarization tornadic debris signatures Part II: Comparisons and caveats. *Electron. J. Operational Meteor.*, **13**, 138–150.

Snyder, J. C., and H. B. Bluestein, 2014: Some considerations for the use of high-resolution mobile radar data in tornado

intensity determination. *Wea. Forecasting*, **29**, 799–827, https://doi.org/10.1175/WAF-D-14-00026.1.

——, ——, G. Zhang, and S. J. Frasier, 2010: Attenuation correction and hydrometeor classification of high-resolution, X-band, dual-polarized mobile radar measurements in severe convective storms. *J. Atmos. Oceanic Technol.*, **27**, 1979–2001, https://doi.org/10.1175/2010JTECHA1356.1.

Umeyama, A. Y., S. M. Torres, and B. L. Cheong, 2017: Bootstrap dual-polarimetric spectral density estimator. *IEEE Trans. Geosci. Remote Sens.*, **55**, 2299–2312, https://doi.org/10.1109/TGRS.2016.2641385.

Van Den Broeke, M. S., 2015: Polarimetric tornadic debris signature variability and debris fallout signatures. *J. Appl. Meteor. Climatol.*, **54**, 2389–2405, https://doi.org/10.1175/JAMC-D-15-0077.1.

——, and S. T. Jauernic, 2014: Spatial and temporal characteristics of polarimetric tornadic debris signatures. *J. Appl. Meteor. Climatol.*, **53**, 2217–2231, https://doi.org/10.1175/JAMC-D-14-0094.1.

Vivekanandan, J., S. M. Ellis, R. Oye, D. S. Zrnić, A. V. Ryzhkov, and J. Straka, 1999: Cloud microphysics retrieval using S-band dual-polarization radar measurements. *Bull. Amer. Meteor. Soc.*, **80**, 381–388, https://doi.org/10.1175/1520-0477(1999)080<0381:CMRUSB>2.0.CO;2.

Wakimoto, R. M., and B. E. Martner, 1992: Observations of a Colorado tornado. Part II: Combined photogrammetric and Doppler radar analysis. *Mon. Wea. Rev.*, **120**, 522–543, https://doi.org/10.1175/1520-0493(1992)120<0522:OOACTP>2.0.CO;2.

——, W. Lee, H. B. Bluestein, C. Liu, and P. H. Hildebrand, 1996: ELDORA observations during VORTEX 95. *Bull. Amer. Meteor. Soc.*, **77**, 1465–1481, https://doi.org/10.1175/1520-0477(1996)077<1465:EODV>2.0.CO;2.

——, N. T. Atkins, and J. Wurman, 2011: The LaGrange tornado during VORTEX2. Part I: Photogrammetric analysis of the tornado combined with single-Doppler radar data. *Mon. Wea. Rev.*, **139**, 2233–2258, https://doi.org/10.1175/2010MWR3568.1.

——, ——, K. M. Butler, H. B. Bluestein, K. Thiem, J. C. Snyder, and J. L. Houser, 2015: Photogrammetric analysis of the 2013 El Reno tornado combined with mobile X-band polarimetric radar data. *Mon. Wea. Rev.*, **143**, 2657–2683, https://doi.org/10.1175/MWR-D-15-0034.1.

——, and Coauthors, 2016: Aerial damage survey of the 2013 El Reno tornado combined with mobile radar data. *Mon. Wea. Rev.*, **144**, 1749–1776, https://doi.org/10.1175/MWR-D-15-0367.1.

WSEC, 2006: A recommendation for an enhanced Fujita scale (EF-scale). Revision 2, Texas Tech University Wind Science and Engineering Center Rep., 111 pp., www.depts.ttu.edu/weweb/pubs/fscale/efscale.pdf.

Wurman, J., and S. Gill, 2000: Finescale radar observations of the Dimmitt, Texas (2 June 1995), tornado. *Mon. Wea. Rev.*, **128**, 2135–2164, https://doi.org/10.1175/1520-0493(2000)128<2135:FROOTD>2.0.CO;2.

Zrnić, D. S., and A. V. Ryzhkov, 1999: Polarimetry for weather surveillance radars. *Bull. Amer. Meteor. Soc.*, **80**, 389–406, https://doi.org/10.1175/1520-0477(1999)080<0389:PFWSR>2.0.CO;2.